Effect of Temperature and Pressure on Structural and Optical Properties of Organic−Inorganic Hybrid Manganese Halides

Yi-Shin Chen, Zhen Bao, Wen-Tse Huang, Agata Lazarowska, Natalia Majewska, Sebastian Mahlik, Grzegorz Leniec, Slawomir M. Kaczmarek, Hsiao-Yu Huang, Chun-I Wu, Di-Jing Huang, and Ru-Shi Liu*

Read Online

ACCESS | Metrics & More | Article Recommendations | SI Supporting Information

ABSTRACT: Organic−inorganic hybrid metal halides have recently attracted attention in the global research field for their bright light emission, tunable photoluminescence wavelength, and convenient synthesis method. This study reports the detailed properties of $(C_{10}H_{16}N)_2MnBr_4$, which emits bright green light with a high photoluminescence quantum yield. Results of powder X-ray diffraction, photoluminescence, thermogravimetric analysis, and Raman spectra show the phase transition of $(C_{10}H_{16}N)_2MnBr_4$ at 430 K. This phase transition was identified as the solid to liquid state of $(C_{10}H_{16}N)_2MnBr_4$. Moreover, the pressure- and temperature-induced relationship between structural and optical properties in $(C_{10}H_{16}N)_2MnBr_4$ can be identified. This investigation provides deep insights into the luminescent properties of metal halide crystals and promotes further research.
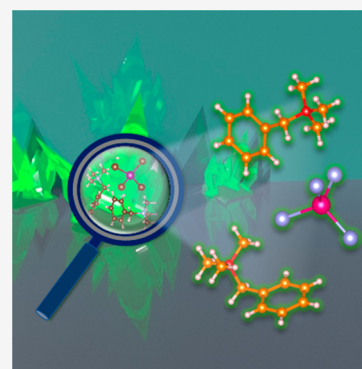
INTRODUCTION

Hybrid metal halides have emerged as a new light-emitting material which possesses many applications covering photovoltaics, laser, and light-emitting diodes (LEDs).[1−4] This series of complexes showed bright emitting light and can be used in organic light-emitting diode (OLED).[5] With the tunable and flexible photoluminescence properties, organic−inorganic materials have been discovered. The formula is $A_mB_nX_y$, where A stands for organic cation, B stands for metals, and X stands for halides, for example, $(C_8H_{20}N_2)PbBr_4$,[6] (3-pyrrolinium)$MnCl_3$,[7] (3AMP)$MnBr_4$,[8] and $(C_9H_{20}N)_2SnBr_4$.[9] Among them, luminescent Mn(II) complexes have attracted more attention than the others due to the less toxicity compared with the lead complexes, much plentiful storage compared with the rare-earth elements, and more stability compared with the tin complexes. The Mn(II) organic−inorganic complexes are divided into two geometries, namely, tetrahedral (green emitting light) and octahedral (red emitting light).[10,11] Most of the studies focused on the T_d geometry of the manganese complexes, which are high-spin with five electrons. The green emission is attributed to the transition from the excited state ($^4T_1$) to the ground state ($^6A_1$) of Mn^{2+} ions.[5] These complexes have excellent photoluminescence quantum efficiency and high thermal stability.[5,12]

In addition to the outstanding photoluminescence properties, these types of complexes also exhibit ferroelectricity. In the previous work, Peng and co-workers mixed $MnBr_2$ with diisopropylamide bromide to obtain the luminescent ferroelectrics (diisopropylammonium)$_2MnBr_4$. It has a high Curie

temperature of 420 K and a photoluminescence quantum yield (PLQY) of 62%.[13] Xiong and co-workers mixed $MnBr_2$ with $[(CH_3)_3NH]Br$ to get $[(CH_3)_3NH]_3(MnBr_3)(MnBr_4)$. It has a Curie temperature of 458 K and a PLQY of 42%.[14] However, the PLQY of the two materials mentioned above is not high among this series of hybrid metal halides and needs to be optimized. In the previous work, $(C_{10}H_{16}N)_2MnBr_4$ exhibited a Curie temperature of 421 K and a PLQY of 72%.[15,16] However, the reversible solid-to-liquid phase transition at around this temperature was seldom considered in this phenomenon. The impact of the pressure on this kind of complex should also be considered. Rodríguez and co-workers described the pressure-induced effects on PL of $MnX_4^{2−}$ and $MnX_6^{4−}$ but did not perform any further high-temperature PL experiments to prove the chemical decomposition of $[(CH_3)_4N]_2MnX_4$ (X: Cl, Br).[17] Zhou and co-workers have done the basic structure research on luminescent properties based on the $(C_{10}H_{16}N)_2MnBr_4$.[16] However, they did not do the deeper research on optical properties.

Herein, we prepared the tetrahedral Mn(II) complex $(C_{10}H_{16}N)_2MnBr_4$ with the convenient solution method for

A

further research. Powder X-ray diffraction (PXRD), electron paramagnetic resonance (EPR), thermogravimetric analysis/differential thermal analysis (TGA/DTA), PL, and Raman spectroscopy were measured to discover the possibilities for detailed investigations of optical properties. For the luminescence properties, $(C_{10}H_{16}N)_2MnBr_4$ emits bright green light under 450 nm excitation and has a phase transition at around 430 K. The PLQY of $(C_{10}H_{16}N)_2MnBr_4$ is 83%, which is higher than that in the previous work. We can conclude that a phase transition occurred at the above-mentioned temperature by research and integration of the spectral properties of XRD, PL, TGA/DTA, and Raman spectra. Pressure-dependent PL spectra reveal that the structural change of $(C_{10}H_{16}N)_2MnBr_4$ associated with a crystal field strength increases due to crystal compression. For the structural properties, temperature-dependent Raman spectra can provide detailed information about the bonding of the complexes. Pressure-dependent Raman spectra can identify the role of organic and inorganic parts in $(C_{10}H_{16}N)_2MnBr_4$.

■ EXPERIMENTAL SECTION

Materials. The materials are manganese(II) bromide (98%, Aldrich), benzyltrimethylammonium bromide (98+%, ACROS), and ethyl ether anhydrous (99%, ECHO).

Synthesis of $(C_{10}H_{16}N)_2MnBr_4$ Crystals. Benzyltrimethylammonium bromide $(C_{10}H_{16}BrN)$ at 10 mmol and manganese(II) bromide $(MnBr_2)$ at 5 mmol were added to an aqueous solution under stirring at 333 K. Light green crystals were obtained in 353 K ovens after 3 days. Finally, the crystals were washed with ethyl ether and dried in a vacuum overnight.

X-ray Powder Diffraction. The obtained $(C_{10}H_{16}N)_2MnBr_4$ powder XRD pattern and temperature-dependent XRD were characterized at the National Synchrotron Radiation Research Center (NSRRC, Taiwan), BL01C2, Hsinchu, Taiwan.

Single-Crystal X-ray Diffraction Data. Single-crystal X-ray diffraction data were collected by a Bruker D8 VENTURE single-crystal XRD equipped with an Oxford Cryostream 800[+] from National Taiwan University.

Photoluminescence Quantum Yield. The quantum yields of the powder $(C_{10}H_{16}N)_2MnBr_4$ were measured by using an absolute PL quantum yield spectrometer (c11347, Hamamatsu).

Room Temperature Photoluminescence Excitation and Photoluminescence Spectra. Photoluminescence spectra (PL) were acquired by using a FluoroMax-4P spectrofluorometer (Horiba) equipped with a 150 W ozone-free xenon lamp as an excitation source and with an R928 Hamamatsu photomultiplier as a detector.

Temperature- and Pressure-Dependent PL. The temperature- and pressure-dependent luminescence spectra were measured by using an Andor SR-750-D1 spectrometer equipped with a CCD camera (DU420A-OE). A Kimmon Koha He−Cd laser with 442 nm was used as the excitation source. The decay profiles were measured by using a PG 401/SH optical parametric generator pumped by a PL2251A pulsed YAG:Nd laser (EKSPLA). The detection part consists of a 2501S grating spectrometer (Bruker Optics) combined with a C4334-01 streak camera (Hamamatsu). The sample was cooled by an APD Cryogenics closed-cycle DE-202 optical cryostat whch allowed the temperature to vary between 10 and 600 K.

High-pressure luminescence measurements were performed in a screw-driven Merrill-Bassett type diamond anvil cell with a 0.5 mm diamond culet diameter.[18] The gasket for the pressure chamber was preindented to around 0.07 mm. A hole with a diameter of 0.2 mm was drilled in the center of the gasket indentation. Polydimethylsiloxane oil was used as the pressure transmitting medium. The pressure was determined based on observing the pressure-induced shift of two luminescence lines (R_1 and R_2) associated with the $^2E \rightarrow {}^4A_2$ transitions in Cr^{3+} ions in a ruby crystal ($Al_2O_3:Cr^{3+}$).[19]

Raman Spectra. Raman spectra were recorded by using a confocal micro-Raman system equipped with a microscope and a Horiba Jobin Yvon Lab Ram Aramis spectrometer with a He−Ne laser. Excitation light was provided at 633 nm with 300 lines/mm grating. Considering the temperature dependence of Raman spectra measurement, the temperature was controlled by using the THMSG600 temperature controller Linkam stage combined with the LNP95 liquid nitrogen cooling pump system to obtain temperatures in the range of −196 to 300 °C.

X-ray Absorption (XAS) and Resonant Inelastic X-ray Scattering (RIXS) Spectra. The obtained XAS and RIXS spectra of $(C_{10}H_{16}N)_2MnBr_4$ were characterized in National Synchrotron Radiation Research Center (NSRRC, Taiwan) Taiwan Photon Source BL41A (Hsinchu, Taiwan).

EPR Spectra. The EPR spectra were recorded at room temperature by using the conventional Bruker X-band ELEXSYS E500 CW spectrometer operating at 9.6 GHz and 0.6 mW microwave power. The magnetic induction ranged from 0 to 1.4 T. The first derivative of the absorption spectrum was recorded as a function of the applied magnetic induction. The EPR-NMR program was used to calculate the spin Hamiltonian parameters (SH).[20] The X-band EPR measurements were conducted at room temperature while the single-crystal sample is rotating around the A- and B-axes. A laboratory axis system was adopted due to the lack of single-crystal orientation. The investigations were made for the axis perpendicular to both microwave and magnetic fields (A-axis). The laboratory B-axis was the crystal growth axis.

Magnetic Susceptibility. Static measurements of the magnetic susceptibility were performed by using the Quantum Design with EverCool Magnetic Property Measurement system MPMS XL-7. The magnetic susceptibility was measured in two modes, namely, zero field cooling (ZFC) and field cooling (FC). The measurements at the entire temperature range from 2 K to room temperature, and magnetic fields up to 30 kOe were recorded. Measurements were performed for a magnetic field $H = 10$ Oe to satisfy the $H/kT \ll 1$ condition. To analyze the above results, the Curie−Weiss law was adopted. The susceptibility data were corrected due to the diamagnetism of a sample holder and the constituent atoms by Pascal's constants.

■ RESULTS AND DISCUSSION

The single-crystal X-ray diffraction (SCXRD) results show that the unit cell parameters of $(C_{10}H_{16}N)_2MnBr_4$ are as follows: $a = 9.5337(11)$ Å, $b = 9.0246(8)$ Å, $c = 15.1273(17)$ Å, $\alpha = \gamma = 90°$, and $\beta = 94.448(10)°$. The other crystal data and experimental details are shown in Table S1. The view of $(C_{10}H_{16}N)_2MnBr_4$ crystal structure along the a-axis is shown in Figure 1a. As shown in Figure 1b, the $[MnBr_4]^{2-}$ anions are isolated from the organic part, namely, $[C_{10}H_{16}N]^+$, which is an individual ion. Thus, $(C_{10}H_{16}N)_2MnBr_4$ is termed zero-dimensional structures (0D) of hybrid metal halides.

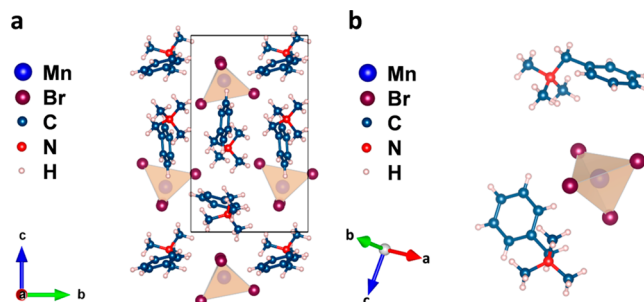**Figure 1.** (a) View of $(C_{10}H_{16}N)_2MnBr_4$ crystal structure along the a-axis. (b) Local structure of $(C_{10}H_{16}N)_2MnBr_4$.

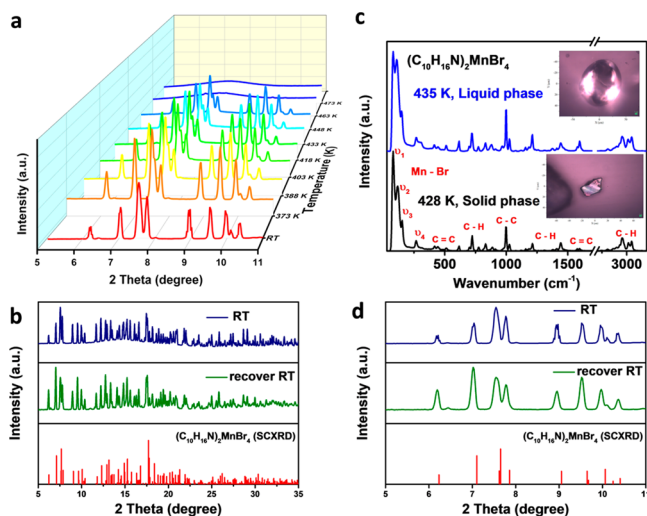The temperature-dependent XRD patterns of $(C_{10}H_{16}N)_2MnBr_4$ are shown in Figure 2a, and the 2D figure

Figure 2. (a) Temperature-dependent X-ray diffraction patterns of $(C_{10}H_{16}N)_2MnBr_4$ from RT to 473 K for the 2θ from 5° to 11°. (b) Comparison of RT, recovery to RT, and calculated XRD patterns of $(C_{10}H_{16}N)_2MnBr_4$. (c) Raman spectra of $(C_{10}H_{16}N)_2MnBr_4$ under excitation with 633 nm. The insets show images of $(C_{10}H_{16}N)_2MnBr_4$ at 428 and 435 K. (d) Magnification of (b) for 2θ from 5° to 11°.

of Figure 2a is shown in Figure S1b. To clearly view the change of the XRD patterns, we only show the 2θ from 5° to 11°, and the complete patterns are shown in Figure S1a. We first measure XRD at room temperature (RT) and various temperatures up to 473 K; eventually, the temperature drops to RT, as shown in Figure 2b. The magnification of Figure 2b for the 2θ from 5° to 11° is shown in Figure 2d. The patterns show that when the temperature reaches 373 K, the background is high due to the strong diffraction at high temperatures. During the heating process, the intensity of the peak starts to decrease at 433 K, and the crystal becomes amorphous at 463 K. We suggest that $(C_{10}H_{16}N)_2MnBr_4$ has a phase transition at around 430 K. These thermally induced changes are reversible, as shown when the temperature recovers to RT. The XRD spectrum of $(C_{10}H_{16}N)_2MnBr_4$ is the same as the original spectrum, as shown in Figure 2b. To check the thermal ability of this compound, the TGA/DTA is measured from RT to 500 K, as shown in Figure S2. An endothermic peak appeared at around 435 K, revealing that a phase transition possibly occurred in this temperature range, which corresponds to the temperature-dependent XRD patterns.

We have studied the phase transition of $(C_{10}H_{16}N)_2MnBr_4$ by a confocal micro-Raman system equipped with a microscope. Figure 2c shows the microscope images and Raman spectra of $(C_{10}H_{16}N)_2MnBr_4$ detected at two temperatures, namely, 428 K (temperature below phase transition that is in a solid state, black curve) and 435 K (temperature above phase transition that is in a liquid state, blue curve), excited with a wavelength of 633 nm. Up to 428 K, the $(C_{10}H_{16}N)_2MnBr_4$ is a solid crystal but starts melting with further temperature increases. Clearly, the phase transition from solid to liquid is observed at 435 K, and the crystal melts into spherical liquid droplets. The vibronic structure related to the inorganic part $[MnBr_4]^{2-}$ is seen below 400 cm^{-1}, and other structures

concerning the organic part $[(C_{10}H_{16}N)_2]$ are seen from 400 to 3200 cm^{-1}. We can attribute some of these structures through comparison with similar compounds.[21−23] The principal bands are assigned to the C−H wagging modes, which can be seen in the range 760−960 cm^{-1}, the C−H stretching modes are in the range 1800−3200 cm^{-1}, the C=C torsion vibrations are at 425 cm^{-1}, and the C=C stretching vibrations are in the range 1620−1660 cm^{-1}. The vibrations of the $[MnBr_4]^{2-}$ in the solid-state $(C_{10}H_{16}N)_2MnBr_4$ are observed at 82 cm^{-1} (ν_1), 118 cm^{-1} (ν_2), 154 cm^{-1} (ν_3), and 267 cm^{-1} (ν_4). The maximum of some vibration lines in the Raman spectra of the liquid phase shifts to the lower wavenumbers together with the change of intensity compared with the solid phase. The most prominent asymmetric bending modes ν_2 and ν_3 shift to 109 and 150 cm^{-1} in solution with an increasing intensity unlike the symmetric bending modes ν_1 observed at 82 cm^{-1} in both phases. According to Gruneisen,[24] the relative change of the position of each vibration to lower frequencies at the temperature of the phase transition indicates an increase in volume. This behavior is expected, as most substances increase their volume during the transition from solid to liquid.

The Tanabe−Sugano diagrams of high-spin Mn^{2+}(d^5) and RT photoluminescence excitation and luminescence spectra of $(C_{10}H_{16}N)_2MnBr_4$ are presented in Figures 3a and 3b. The Commission Internationale de L'Eclairage (CIE) 1931 color space of $(C_{10}H_{16}N)_2MnBr_4$ is shown in Figure S3. The PL spectrum (green curve in Figure 3b) shows a narrow band with

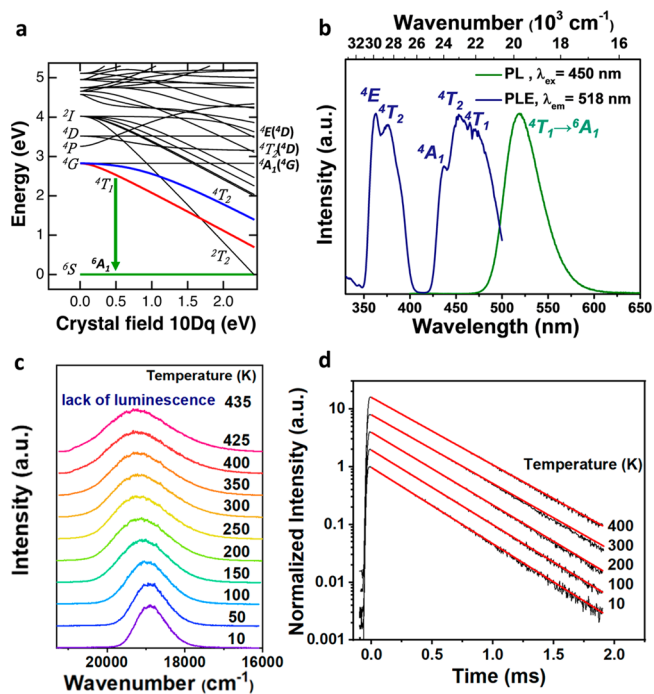**Figure 3.** (a) Tanabe−Sugano diagram of high-spin Mn^{2+} (d^5) calculated by using the parameters from RIXS measurements. The green arrow corresponds to the emission. (b) Photoluminescence excitation spectra upon observation at maximum luminescence and emission spectra upon excitation at 450 nm of $(C_{10}H_{16}N)_2MnBr_4$ (c) Temperature-dependent luminescence spectra of $(C_{10}H_{16}N)_2MnBr_4$ under 450 nm excitation. (d) Temperature-dependent luminescence decay kinetics of $(C_{10}H_{16}N)_2MnBr_4$ (excited by the 450 nm laser line). The decay profiles are normalized to the maximum emission and stacking to show the clarity of this image.

a maximum at 518 nm; this is associated with the transition from the lowest excited state ($^4T_1$) to the ground state ($^6A_1$) in Mn^{2+} ions (Figure 3a). The photoluminescence excitation (PLE) spectrum (blue curve in Figure 3b) monitored at 518 nm shows two main groups of transition within the $3d^5$ configuration of Mn^{2+} from the ground state ($^6A_1$) to the $^4T_1(^4G)$, $^4T_2(^4G)$, $^4A_1(^4G)$ (from 425 to 500 nm), $^4T_2(^4D)$, and $^4E(^4D)$ (from 350 to 400 nm) energy levels. All the d−d transitions in Mn^{2+} are parity- and spin-forbidden. Thus, the absorption and emission efficiency of Mn^{2+} are expected to be relatively low. However, the organic−inorganic compound $(C_{10}H_{16}N)_2MnBr_4$ allows Mn^{2+} to be fully incorporated into the crystal structure, enhancing the absorption efficiency. Simultaneously, $[MnBr_4]^{2-}$ tetrahedra are isolated from each other by the $[(C_{10}H_{16}N)_2]$ organic cations, which prevent nonradiative losses induced by the energy transfer between Mn^{2+} ions. This leads to excellent photoluminescent properties with a PLQY of 83%. The energy transitions seen in the excitation and emission spectra (described in Figure 3a) are collected in Table S2. To obtain the crystal field parameters of Mn^{2+}, we performed measurements of Mn L_3-edge resonant inelastic X-ray scattering (RIXS).

Figure 4 plots Mn L_3-edge X-ray absorption (XAS) and RIXS spectra. Through comparing the measurement data with multiplet calculations, we found that both XAS and RIXS spectra can be explained by calculations using $10Dq = -0.5$ eV for the crystal field of tetrahedral symmetry. We considered Mn^{2+} in octahedral symmetry with a negative crystal field $10Dq$ to mimic the electronic structure of tetrahedral Mn^{2+}. The 3d−3d multiplet interactions are described with the Slater integrals; their values were set to 70% of Hartree−Fock values. With these parameters, we calculated the Tanabe−Sugano diagram of high-spin Mn^{2+} in $(C_{10}H_{16}N)_2MnBr_4$ presented in Figure 3a, which shows that the $^4T_1 \rightarrow {}^6A_1$ transition energy agrees with the PL energy. Further RIXS calculations will be conducted in the future to clarify the distortions of Mn.

To check the temperature-dependent photoluminescent properties, we tested the emission spectra of $(C_{10}H_{16}N)_2MnBr_4$ under 450 nm excitation at temperatures in the range 10−435 K, as shown in Figure 3c. The emission band strongly depends on the temperature and shifts to shorter wavelengths with increasing temperature, from 18870 cm^{-1} (530 nm) at 10 K to 19300 cm^{-1} (518 nm) at 425 K. This blue-shift can be due to emission from thermally occupied higher (vibrational) levels together with the thermally induced lattice expansion, which decreases the crystal field strength. The full width at half-maximum (FWHM) of the emission band increases significantly from 920 to 1887 cm^{-1}, as shown in Figure S4.

The strong luminescence from Mn^{2+} ions (under 450 nm excitation) suddenly disappears at 435 K (Figure 3c) and is completely quenched at higher temperatures. The abrupt change (lack of luminescence) in PL spectra observed at 435 K is related to the melting of $(C_{10}H_{16}N)_2MnBr_4$ crystal. Breaking of weak hydrogen bonds C−H···Br upon melting explained why no appreciable Mn^{2+} luminescence could be detected in a liquid state. Upon melting, the liberation of tetrahedra from organic part $[(C_{10}H_{16}N)_2]$ leads to the activation of translation mobility of $[MnBr_4]^{2-}$ tetrahedra. This allows collisions of the excited $[MnBr_4]^{2-}$ with other molecules and consequently enhances the nonradiative recombination rate. When the temperature decreases, a strong green luminescence band reappears.
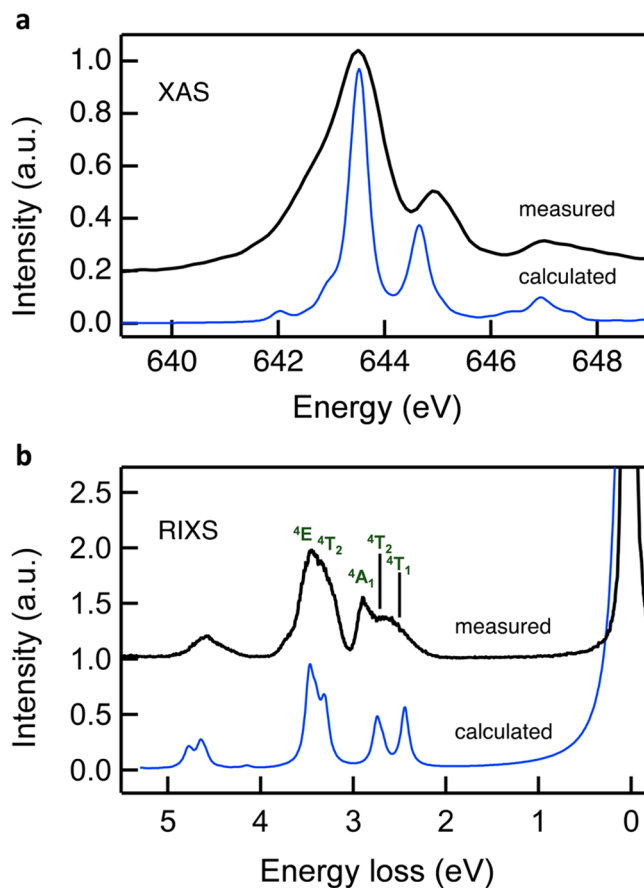

Figure 4. XAS and RIXS measurements of $(C_{10}H_{16}N)_2MnBr_4$. (a) L_3-edge X-ray absorption spectrum in comparison with multiplet calculations. The XAS spectrum was measured by the total fluorescence yield method. (b) RIXS spectrum recorded with the incident X-ray energy tuned to the incident X-ray of energy 643.5 eV with σ polarization. Both calculated XAS and RIXS spectra are plotted in blue. Multiple calculations of tetrahedral Mn^{2+} were performed by using Quanty (http://www.quanty.org/).

The normalized luminescence decay curves of $(C_{10}H_{16}N)_2MnBr_4$ in the temperature range 10−400 K are shown in Figure 3d. The decay curves are single-exponential at all temperatures studied. Thus, the single-exponential formula is used to fit the experimental data:

$$I(t) = I_0 e^{-t/\tau} \tag{1}$$

where $I(t)$ is the intensity of the emission at time t, I_0 is the initial intensity, and τ is the decay time of the luminescence. The decay time calculated as a function of temperature is presented in Figure S5. Generally, the Mn^{2+} luminescence decay in dielectric hosts is characterized by a relatively long lifetime from single to tens of milliseconds because the observed $^4T_1 \rightarrow {}^6A_1$ transition is forbidden by both the combination of the spin selection rule and the parity selection rule.[25] However, in the ferroelectric material $(C_{10}H_{16}N)_2MnBr_4$, the luminescence lifetime is much shorter than expected, and its value is 0.33 ms in 10 K. Such a short lifetime can be explained by lifting the inversion symmetry around the Mn^{2+} ion, which is coordinated with four Br ions, to give a distorted tetrahedron. The decay time slightly increases from 0.33 to 0.36 ms with increasing temperature from 10 to 350 K, as shown in Figure S5. This effect can be explained by the decreasing probability of radiative transition,

which is significantly dependent on the local surroundings of the Mn^{2+} ion. When the local symmetry distortion is reduced, the transition probability should increase, lengthening the decay time. This effect is visible in our measurements. With increasing temperature, the symmetry of the local Mn^{2+} environment changes, increasing the decay time value. This is in line with the results obtained in the EPR measurement, which show that the axial distortion of the surrounding Mn^{2+} ions decreases with increasing temperature.

The pressure-dependent luminescence spectra of the $(C_{10}H_{16}N)_2MnBr_4$ measured at RT are shown in Figure 5a.

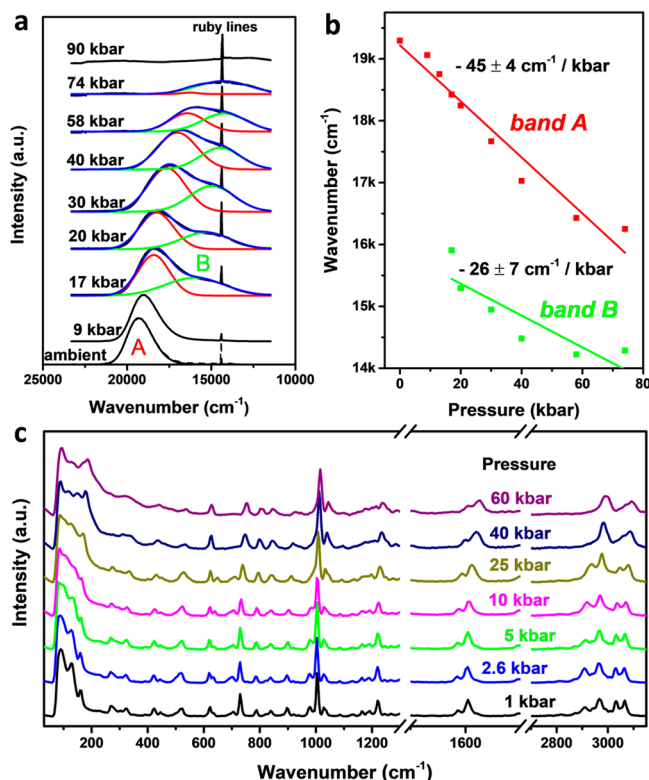**Figure 5.** (a) Pressure-dependent luminescence spectra of $(C_{10}H_{16}N)_2MnBr_4$ are measured at RT and are excited by 442 nm laser light. The spectra are normalized to the maximum of the Mn^{2+} luminescence. Band A is marked as the green line, and band B is marked as the red line. (b) Positions of the luminescence peaks of A and B as functions of pressure for $(C_{10}H_{16}N)_2MnBr_4$. (c) Raman spectra of $(C_{10}H_{16}N)_2MnBr_4$ as a function of pressure.

The narrow emission band, which is at 520 nm at ambient pressure, is marked as A in Figure 5a, and it shifts with higher pressure to the lower energy. At ~17 kbar, a low-intensity emission band (marked as B in Figure 5a) appears in the emission spectrum, with the maximum at 630 nm. Band A is marked as the green line, and band B is marked as the red line. Further increasing the pressure above 17 kbar causes the luminescence intensity of band A to decrease, causing a relative increase in band B up to 74 kbar. At pressures above 90 kbar, only the low-intensity luminescence band B remains. The value of decay time of band B (which is 0.35 ms, as shown in Figure S6) suggests that these emissions originate from Mn^{2+} ions. There are two geometries, namely, the green (tetrahedrally coordinated) and red (octahedrally coordinated) luminescence emission from the $^4T_1(G)$ level, observed due to the local coordination environment of Mn^{2+}. The manganese dihalide

$MnBr_2$ precursor, used as a chemical reaction of $(C_{10}H_{16}N)_2MnBr_4$ compound, shows a red luminescence because Mn^{2+} ions occupy slightly trigonally distorted octahedral sites.[26] The small fraction of the $MnBr_2$ in the final $(C_{10}H_{16}N)_2MnBr_4$ compound could explain the relatively low intensity of the red luminescence band B. The emission bands A and B shift approximately linearly with pressure to the lower energy, and the pressure coefficients are -45 ± 4 cm^{-1}/kbar for band A and -26 ± 7 cm^{-1}/kbar for band B, as shown in Figure 5b. Such shifts related to the decrease of the energy of the first excited level ($^4T_{1g}$) for Mn^{2+} (as shown in Figure 3a) are expected, as the crystal field strength increases with pressure because of the compression of the crystal. The same as in the temperature-dependent XRD and temperature-dependent PL, pressure-induced changes are reversible. After the pressure release, the emission spectrum of $(C_{10}H_{16}N)_2MnBr_4$ is the same as before compression.

The decay kinetics of the band A luminescence is single-exponential at ambient pressure, as shown in Figure 3d. When pressure is applied at ~4 kbar, the luminescence decay curves (see Figure S6a) become nonexponential and faster; therefore, only the average luminescence decay times could be determined. The average decay times were calculated via the formula

$$\bar{\tau} = \frac{\int_0^\infty t\, I(t)\, \mathrm{d}t}{\int_0^\infty I(t)\, \mathrm{d}t} \qquad (2)$$

where $I(t)$ represent the decay curves. The calculated average decay times are presented in Figure S6c (red squares). The luminescence decay shortening is observed in two steps. First, a dramatic decrease occurred below 20 kbar. Shortening of the decay time together with the decrease of luminescence intensity of band A up to 20 kbar indicates the presence of an efficient luminescence quenching process that is activated under pressure. A further increase in the pressure slightly shortened the average decay time, with the emission intensity gradually becoming lower.

The decay profiles of B luminescence, which appears at 17 kbar, are also nonexponential; therefore, the average decay times were calculated via eq 2 and presented in Figure S6c (green squares). The shortening of the decay time was accompanied by a decrease in the intensity of the emission, which resulted in it. At pressure levels higher than 74 kbar, the luminescence of the sample became too weak to be measured.

To investigate the pressure-induced quenching of $[MnBr_4]^{2-}$ tetrahedra in detail and the role of their interaction with the organic part, we conducted high-pressure Raman experiments at RT. With increasing pressure, the energy of all Raman peaks increases, as shown in Figure 5c. Moreover, Mn−Br vibrational modes (below 400 cm^{-1}) with 2 times larger pressure coefficients than other vibrations are related to the organic parts (400−3200 cm^{-1}). This shift is ascribed to lattice contraction. The calculation of the pressure shift of the $(C_{10}H_{16}N)_2MnBr_4$ of Raman spectra is shown in Figure S7. In $(C_{10}H_{16}N)_2MnBr_4$ material, $[MnBr_4]^{2-}$ tetrahedra are isolated by the $[(C_{10}H_{16}N)_2]$ organic cations, which provide a sufficiently long Mn−Mn distance to prevent nonradiative losses induced by the energy transfer between Mn^{2+} ions at ambient pressure.[27] When pressure is applied on the $(C_{10}H_{16}N)_2MnBr_4$, the compressions leading to the distance between the closest Mn ions are sufficiently low for an effective

energy process, consequently quenching Mn^{2+} luminescence. Moreover, $[MnBr_4]^{2-}$ tetrahedra start being distorted with increasing pressure. Consequently, the nonuniform distribution of Br ions around Mn is expected to give rise to an observed broadening of the luminescence band together with a tremendous red-shift of the luminescence band maximum. The organic part maintained well-defined features in the spectrum up to 25 kbar. However, at ~40 kbar pressure, some high-frequency vibrational lines disappear and another starts to broaden, suggesting that the distortion of the organic part plays a role. High-pressure Raman spectra indicate that the inorganic layer is first distorted to provide enough space to accommodate bulky organic molecules. Second, at higher pressures (~40 kbar), organic cations start to be distorted gradually. Such a sequential distortion mechanism under compression has also been observed recently in 2D organic–inorganic perovskite structures.[28] Upon decompression, $(C_{10}H_{16}N)_2MnBr_4$ is restored to its original state, which is consistent with the XRD and PL analysis. The structural memory effect is due to flexible bulky organic cations, which can act as templates for the recovery process.[29]

Temperature-dependent EPR spectra show that the changes in the fine structure of the EPR spectrum are caused by the changes in the surrounding of the Mn^{2+} ions. Variations in axial distortion (D value from eq 1 in the Supporting Information) indicate (as shown in the inset of Figure 6a) that distortion of the surrounding Mn^{2+} ions increases with decreasing temperature. Below 140 K, the values of the D parameter slightly increase, and the g_z parameter begins to increase with decreasing temperature, causing significant axial anisotropy of the Mn^{2+} ions' nearest surroundings. Hysteresis loop measurements for $(C_{10}H_{16}N)_2MnBr_4$ in a powder and crystal form at two different temperatures were performed by the SQUID device, as shown in Figure 6b. This is a typical magnetic hysteresis loop usually observed for paramagnetic compounds. Magnetic anisotropy is not observed for both kinds of $(C_{10}H_{16}N)_2MnBr_4$. The investigated samples show nearly zero remanences and coercion fields (B_r and H_c, respectively). For a single crystal $B_r = 2.1 \times 10^{-4}$ emu/g and $H_c = -1.1$ mT, while for a powder $B_r = 1.99 \times 10^{-4}$ emu/g and $H_c = -1.3$ mT. The values are typical for paramagnetic Mn^{2+} ions. Analysis of the EPR results and EPR spectra is presented in the Supporting Information.

CONCLUSION

In conclusion, we have successfully synthesized the organic–inorganic compound $(C_{10}H_{16}N)_2MnBr_4$. The emission peak is at 518 nm with 83% of the PLQY. $(C_{10}H_{16}N)_2MnBr_4$ has a phase transition at 430 K, which is shown through XRD, TGA, PL, and Raman spectra comparison. When the temperature is back to the ambient condition, $(C_{10}H_{16}N)_2MnBr_4$ is restored to its original state. From the pressure-induced PL spectra, we could clearly see that the change of the $(C_{10}H_{16}N)_2MnBr_4$ associated with a crystal field strength increases because of the compression of the crystal. Thus, a red-shift occurs. Moreover, we can determine the role of the organic and inorganic parts separately. We believe that this kind of hybrid metal halides with high PLQY, tunable photoluminescence, and high thermal stability will be used as emitting materials in the future.
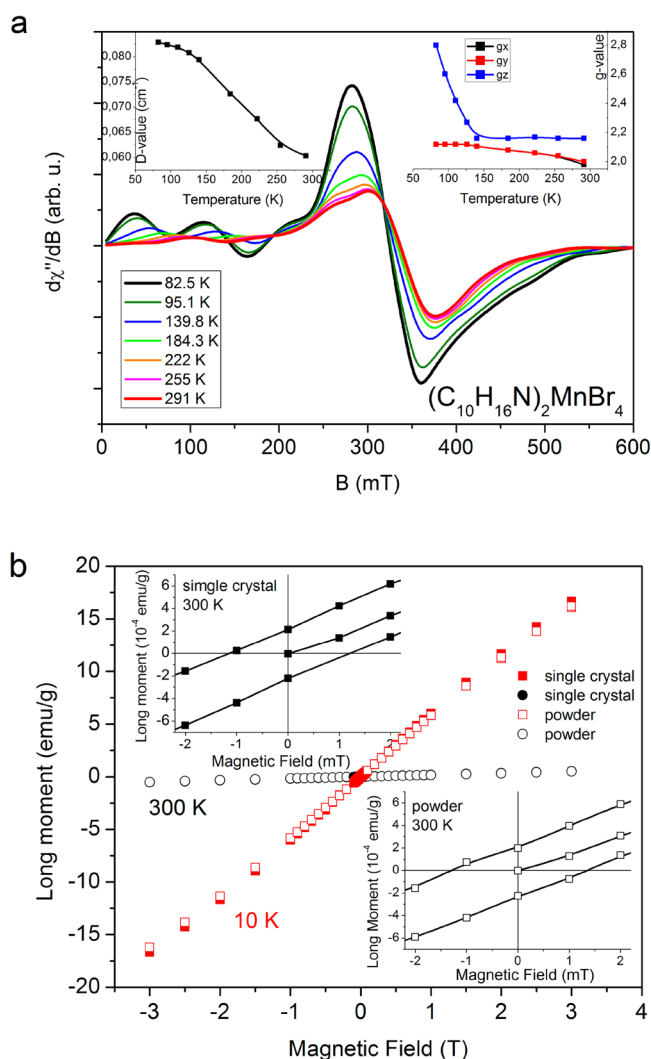

Figure 6. (a) Temperature-dependent EPR spectrum for $(C_{10}H_{16}N)_2MnBr_4$. The inset presents the temperature dependence of changes in the values of parameters D (left side) and g (right side). (b) Hysteresis loops measured for $(C_{10}H_{16}N)_2MnBr_4$ single crystal and powder at 10 and 300 K.

ASSOCIATED CONTENT

Supporting Information

The Supporting Information is available free of charge at https://pubs.acs.org/doi/10.1021/acs.inorgchem.1c03630.

> Optical properties, further temperature-dependent PL properties, pressure-dependent PL properties, electron paramagnetic resonance, thermogravimetric analysis/differential thermal analysis, Raman, X-ray absorption, and resonant inelastic X-ray scattering (PDF)

Accession Codes

CCDC 2124253 contains the supplementary crystallographic data for this paper. These data can be obtained free of charge via www.ccdc.cam.ac.uk/data_request/cif, or by emailing data_request@ccdc.cam.ac.uk, or by contacting The Cambridge Crystallographic Data Centre, 12 Union Road, Cambridge CB2 1EZ, UK; fax: +44 1223 336033.

■ AUTHOR INFORMATION

Corresponding Author

Ru-Shi Liu − *Department of Chemistry, National Taiwan University, Taipei 106, Taiwan; Advanced Research Center of Green Materials Science and Technology, National Taiwan University, Taipei 106, Taiwan;* ◉ orcid.org/0000-0002-1291-9052; Email: rsliu@ntu.edu.tw

Authors

Yi-Shin Chen − *Department of Chemistry, National Taiwan University, Taipei 106, Taiwan*

Zhen Bao − *Department of Chemistry, National Taiwan University, Taipei 106, Taiwan;* ◉ orcid.org/0000-0001-6759-1261

Wen-Tse Huang − *Department of Chemistry, National Taiwan University, Taipei 106, Taiwan*

Agata Lazarowska − *Institute of Experimental Physics, Faculty of Mathematics, Physics and Informatics, University of Gdańsk, 80-308 Gdańsk, Poland*

Natalia Majewska − *Institute of Experimental Physics, Faculty of Mathematics, Physics and Informatics, University of Gdańsk, 80-308 Gdańsk, Poland;* ◉ orcid.org/0000-0002-1933-0355

Sebastian Mahlik − *Institute of Experimental Physics, Faculty of Mathematics, Physics and Informatics, University of Gdańsk, 80-308 Gdańsk, Poland; Graduate School of Human and Environmental Studies, Kyoto University, Kyoto 606-8501, Japan;* ◉ orcid.org/0000-0002-9514-049X

Grzegorz Leniec − *Department of Technical Physics, Faculty of Mechanical Engineering and Mechatronics, West Pomeranian University of Technology in Szczecin, 70-311 Szczecin, Poland*

Sławomir M. Kaczmarek − *Department of Technical Physics, Faculty of Mechanical Engineering and Mechatronics, West Pomeranian University of Technology in Szczecin, 70-311 Szczecin, Poland*

Hsiao-Yu Huang − *National Synchrotron Radiation Research Center, Hsinchu 300, Taiwan*

Chun-I Wu − *Graduate Program in Science and Technology of Synchrotron Light Source, National Tsing Hua University, Hsinchu 300, Taiwan*

Di-Jing Huang − *National Synchrotron Radiation Research Center, Hsinchu 300, Taiwan*

Complete contact information is available at:
https://pubs.acs.org/10.1021/acs.inorgchem.1c03630

Author Contributions

Y.-S.C. and Z.B. contributed equally to this work. The synthesis was conducted by Y.S.C., and characterization of XRD and PLQY was done by Y.S.C., Z.B., and W.T.H. The characterization of PL and Raman was done by A.L., N.M., and S.M. The characterization of EPR and magnetic susceptibility was done by G.L. and S.M.K. The XAS and RIXS were done by H.U.H., C.I.W., and D.J.H. The manuscript was written by Y.S.C. with input from all authors. This research was supervised by R.S.L.

Notes

The authors declare no competing financial interest.

■ REFERENCES

(1) Bhandari, K. P.; Ellingson, R. J. An Overview of Hybrid Organic−Inorganic Metal Halide Perovskite Solar Cells. *A Comprehensive Guide to Solar Energy Systems* **2018**, 233−254.

(2) Brenner, P.; Stulz, M.; Kapp, D.; Abzieher, T.; Paetzold, U. W.; Quintilla, A.; Howard, I. A.; Kalt, H.; Lemmer, U. Highly Stable Solution Processed Metal-Halide Perovskite Lasers on Nanoimprinted Distributed Feedback Structures. *Appl. Phys. Lett.* **2016**, *109*, 141106.

(3) Cho, H.; Jeong, S.-H.; Park, M.-H.; Kim, Y.-H.; Wolf, C.; Lee, C.-L.; Heo, J. H.; Sadhanala, A.; Myoung, N.; Yoo, S.; et al. Overcoming the Electroluminescence Efficiency Limitations of Perovskite Light-Emitting Diodes. *Science* **2015**, *350*, 1222−1225.

(4) Stranks, S. D.; Snaith, H. J. Metal-Halide Perovskites for Photovoltaic and Light-Emitting Devices. *Nat. Nanotechnol.* **2015**, *10*, 391−402.

(5) Xu, L. J.; Sun, C. Z.; Xiao, H.; Wu, Y.; Chen, Z. N. Green-Light-Emitting Diodes Based on Tetrabromide Manganese (II) Complex through Solution Process. *Adv. Mater.* **2017**, *29*, 1605739.

(6) Su, B.; Molokeev, M. S.; Xia, Z. Unveiling Mn^{2+} Dopant States in Two-Dimensional Halide Perovskite toward Highly Efficient Photoluminescence. *J. Phys. Chem. Lett.* **2020**, *11*, 2510−2517.

(7) Ye, H.-Y.; Zhou, Q.; Niu, X.; Liao, W.-Q.; Fu, D.-W.; Zhang, Y.; You, Y.-M.; Wang, J.; Chen, Z.-N.; Xiong, R.-G. High-Temperature Ferroelectricity and Photoluminescence in a Hybrid Organic−Inorganic Compound: (3-Pyrrolinium)$MnCl_3$. *J. Am. Chem. Soc.* **2015**, *137*, 13148−13154.

(8) Mao, L.; Guo, P.; Wang, S.; Cheetham, A. K.; Seshadri, R. Design Principles for Enhancing Photoluminescence Quantum Yield in Hybrid Manganese Bromides. *J. Am. Chem. Soc.* **2020**, *142*, 13582−13589.

(9) Zhou, C.; Lin, H.; Shi, H.; Tian, Y.; Pak, C.; Shatruk, M.; Zhou, Y.; Djurovich, P.; Du, M. H.; Ma, B. A Zero-Dimensional Organic Seesaw-Shaped Tin Bromide with Highly Efficient Strongly Stokes-Shifted Deep-Red Emission. *Angew. Chem.* **2018**, *130*, 1033−1036.

(10) Morad, V.; Cherniukh, I.; Pöttschacher, L.; Shynkarenko, Y.; Yakunin, S.; Kovalenko, M. V. Manganese (II) in Tetrahedral Halide Environment: Factors Governing Bright Green Luminescence. *Chem. Mater.* **2019**, *31*, 10161−10169.

(11) Zhou, Q.; Dolgov, L.; Srivastava, A. M.; Zhou, L.; Wang, Z.; Shi, J.; Dramićanin, M. D.; Brik, M. G.; Wu, M. Mn^{2+} and Mn^{4+} Red Phosphors: Synthesis, Luminescence and Applications in WLEDs. A review. *J. Mater. Chem. C* **2018**, *6*, 2652−2671.

(12) Su, B.; Molokeev, M. S.; Xia, Z. Mn^{2+}-Based Narrow-Band Green-Emitting Cs_3MnBr_5 Phosphor and the Performance Optimization by Zn^{2+} Alloying. *J. Mater. Chem.* **2019**, *7*, 11220−11226.

(13) Jiang, C.; Zhong, N.; Luo, C.; Lin, H.; Zhang, Y.; Peng, H.; Duan, C.-G. (Diisopropylammonium)$_2MnBr_4$: A Multifunctional Ferroelectric with Efficient Green-Emission and Excellent Gas Sensing Properties. *Chem. Commun.* **2017**, *53*, 5954−5957.

(14) Wei, Z.; Liao, W.-Q.; Tang, Y.-Y.; Li, P.-F.; Shi, P.-P.; Cai, H.; Xiong, R.-G. Discovery of an Antiperovskite Ferroelectric in [(CH$_3$)$_3$NH]$_3$(MnBr$_3$)(MnBr$_4$). *J. Am. Chem. Soc.* **2018**, *140*, 8110−8113.

(15) Fu, H.; Jiang, C.; Lao, J.; Luo, C.; Lin, H.; Peng, H.; Duan, C.-G. An Organic−Inorganic Hybrid Ferroelectric with Strong Luminescence and High Curie Temperature. *CrystEngComm.* **2020**, *22*, 1436−1441.

(16) Cai, X.-W.; Zhao, Y.-Y.; Li, H.; Huang, C.-P.; Zhou, Z. Lead-Free/Rare Earth-Free Green-Light-Emitting Crystal Based on Organic-Inorganic Hybrid $[(C_{10}H_{16}N)_2][MnBr_4]$ with High Emissive Quantum Yields and Large Crystal Size. *J. Mol. Struct.* **2018**, *1161*, 262−266.

(17) Rodríguez-Lazcano, Y.; Nataf, L.; Rodríguez, F. Pressure-Induced Transformation from Isolated MnX_4 (Td) to Exchange-Coupled MnX_6 (Oh) in A_2MnX_4 (X: Cl, Br) Crystals. Structural Correlations by Time-Resolved Spectroscopy. *J. Lumin.* **2009**, *129*, 2000−2003.

(18) Merrill, L.; Bassett, W. A. Miniature Diamond Anvil Pressure Cell for Single Crystal X-Ray Diffraction Studies. *Rev. Sci. Instrum.* **1974**, *45*, 290−294.

(19) Piermarini, G. J.; Block, S.; Barnett, J.; Forman, R. Calibration of the pressure dependence of the R 1 ruby fluorescence line to 195 kbar. *J. Appl. Phys.* **1975**, *46*, 2774−2780.

(20) Mombourquette, M.; Weil, J.; McGavin, D. EPR-NMR user's manual. Department of Chemistry, University of Saskatchewan, Saskatoon, SK, Canada, 1996.

(21) Hamdi, M.; Oueslati, A.; Chaabane, I.; Hlel, F. Characterization and Electrical Properties of $[C_6H_9N_2]_2CuCl_4$ Compound *Int. Sch. Res. Notices.* **2012**, *2012*.

(22) Mao, W.; Wang, J.; Hu, X.; Zhou, B.; Zheng, G.; Mo, S.; Li, S.; Long, F.; Zou, Z. Synthesis, Crystal Structure, Photoluminescence Properties of Organic-Inorganic Hybrid Materials Based on Ethyl-enediamine Bromide. *J. Saudi Chem. Soc.* **2020**, *24*, 52−60.

(23) Yadav, R.; Swain, D.; Kundu, P. P.; Nair, H. S.; Narayana, C.; Elizabeth, S. Dielectric and Raman Investigations of Structural Phase Transitions in $(C_2H_5NH_3)_2CdCl_4$. *Phys. Chem. Chem. Phys.* **2015**, *17*, 12207−12214.

(24) Lucazeau, G. Effect of Pressure and Temperature on Raman Spectra of Solids: Anharmonicity. *J. Raman Spectrosc.* **2003**, *34*, 478−496.
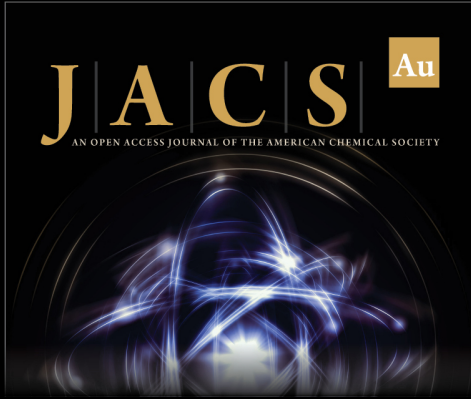
(25) Vink, A.; De Bruin, M.; Roke, S.; Peijzel, P.; Meijerink, A. Luminescence of Exchange Coupled Pairs of Transition Metal Ions. *J. Electrochem. Soc.* **2001**, *148*, E313.

(26) Ronda, C.; Siekman, H.; Haas, C. Photoluminescence and Absorption of $MnCl_2$, $MnBr_2$ and MnI_2. *Physica B+C* **1987**, *144*, 331−340.

(27) Zhou, G.; Liu, Z.; Huang, J.; Molokeev, M. S.; Xiao, Z.; Ma, C.; Xia, Z. Unraveling the Near-Unity Narrow-Band Green Emission in Zero-Dimensional Mn^{2+}-Based Metal Halides: A Case Study of $(C_{10}H_{16}N)_2Zn_{1−x}Mn_xBr_4$ Solid Solutions. *J. Phys. Chem. Lett.* **2020**, *11*, 5956−5962.

(28) Zhang, L.; Wu, L.; Wang, K.; Zou, B. Pressure-Induced Broadband Emission of 2D Organic−Inorganic Hybrid Perovskite $(C_6H_5C_2H_4NH_3)_2PbBr_4$. *Adv. Sci.* **2019**, *6*, 1801628.

(29) Lü, X.; Wang, Y.; Stoumpos, C. C.; Hu, Q.; Guo, X.; Chen, H.; Yang, L.; Smith, J. S.; Yang, W.; Zhao, Y. Enhanced Structural Stability and Photo Responsiveness of $CH_3NH_3SnI_3$ Perovskite Via Pressure-Induced Amorphization and Recrystallization. *Adv. Mater.* **2016**, *28*, 8663−8668.